A New Diagnostic Model and Improved Prediction Algorithm for the Heights of Evaporation Ducts

Yanbo Mai[1], Zheng Sheng[1,2]*, Hanqing Shi[1], Chaolei Li[3], Lihang Liu[4], Qixiang Liao[1], Wei Zhang[1] and Shudao Zhou[1,2]

[1] College of Meteorology and Oceanography, National University of Defense Technology, Nanjing, China, [2] Collaborative Innovation Center on Forecast and Evaluation of Meteorological Disasters, Nanjing University of Information Science and Technology, Nanjing, China, [3] School of Automation, Southeast University, Nanjing, China, [4] Wuxi First Research Institute, Wuxi, China

This paper develops a new method for the diagnosis and prediction of the evaporation duct heights on the sea, which has certain reference significance for the study of the evaporation ducts. Based on traditional diagnostic and predictive models of evaporation duct heights, a new diagnostic model is proposed. By determining the overall Richardson number R_{ib}, the Monin-Obukhov (M-O) length L and the wind speed characteristic parameter u_*, temperature characteristic parameter θ_* and humidity characteristic parameters q_* are calculated, and then the evaporation duct height is diagnosed. Taking the diagnosed heights as a time series, and using the support vector regression (SVR) algorithm improved by a simulated annealing operator, then the time series is analyzed by taking three consecutive sample steps as input and the next sample step as output in order to develop an algorithm for predicting future heights. Finally, the prediction results are compared with those from the traditional auto-regressive (AR) algorithm and classical SVR algorithm to identify the advantages and disadvantages of the improved SVR algorithm. The results show that the root-mean-square error (RMSE) of the traditional AR, the classical SVR and the improved SVR algorithms is 0.60, 0.45, and 0.38, and the mean absolute percentage error (MAPE) of the three algorithms is 7.79%, 6.10% and 4.78%, respectively. The prediction error of the improved SVR algorithm is 37% less than that of the traditional AR algorithm and 15% less than that of the classical SVR algorithm, signifying an improvement in its prediction capability.

Keywords: evaporation duct heights, new diagnostic height model, AR algorithm, improved SVR algorithm, time series

INTRODUCTION

The propagation of electromagnetic waves in the atmosphere is affected not only by absorption and scattering by molecules and aerosol particles but also by refraction (Kang et al., 2014). Abnormal refraction, such as negative refraction, super refraction, and trapping refraction, can cause abnormal propagation of electromagnetic waves (Kang et al., 2014). Under trapping refraction conditions, part of the electromagnetic wave is captured within a certain thickness of atmosphere and propagates back and forth between the upper and lower layers, just like waves propagating in a metal pipe; Regions of atmosphere causing this sort of propagation are called atmospheric ducts

(Kang et al., 2014). There are four kinds of atmospheric ducts: surface ducts, surface-based ducts, elevated ducts, and evaporation ducts (Kang et al., 2014). Evaporation ducts often appear close to the sea surface and it is formed by the evaporation of sea water, which leads to the rapid change of humidity in the vertical direction, and then produces the evaporation ducts. The evaporation ducts have an important influence on the propagation of electromagnetic waves, so they are a vital factor affecting the communication systems of ships and low altitude airborne radar (Shi et al., 2019). The height of an evaporation duct refers to its top height, which is numerically equal to the thickness of the evaporation duct layer (Ivanov et al., 2007). It is the key parameter in determining the refractive index profile of the atmosphere in lower layers and has an important reference significance for the propagation loss of electromagnetic waves. Babin et al. (1997) proposed and tested a new model that uses recently refined bulk similarity expressions developed for the determination of the ocean surface energy budget in the Tropical Ocean Global Atmosphere Coupled Ocean-Atmosphere Response Experiment. Tian et al. (2009a) studied the applicability of evaporation duct Model A in Chinese sea areas by using modified refractivity profiles and meteorological data measured during recent years. To evaluate a method for detecting evaporation ducts, Yang et al. (2016) used hydrological and meteorological data from the South China Sea to compare and analyze measured and predicted evaporation duct heights. Babin and Dockery (2002) developed a wave-riding catamaran with a mast-traveling sensor package (profiling buoy) to generate time-averaged modified refractivity (M) profiles that were then compared with those determined from four evaporation duct models based on the surface layer theory of Liu, Katsaros, and Businger (LKB). Burk et al. (2003) investigated the conditions under which atmospheric island wakes form leeward of Kauai, Hawaii, by using idealized numerical simulations and real forecast data from the U.S. Navy's Coupled Ocean-Atmosphere Mesoscale Prediction System (COAMPS). Tian et al. (2009b) analyzed model sensitivity to air-sea temperature difference, wind speed and relative humidity, and studied the applicability of their model in semitropical sea areas using measured data from recent years. Based on a theoretical derivation, Sheng and Huang (2009, 2010) used simulated and measured radar echo data to retrieve evaporation duct parameters, and analyzed the inversion results and the anti-noise capability of the inversion system. Zhang et al. (2016) and Xie et al. (2017) analyzed the variation of arctic polar vortex in the stratosphere, which may affect the generation of atmospheric ducts. Mai et al. (2020) studied the spatiotemporal distribution of atmospheric ducts in Alaska. Li et al. (2014) proposed a non-iterative scheme using multiple regression to produce similar results to those from classical iterative computation. Liu et al. (2019) compared the sensitivity of four evaporation duct prediction models to meteorological factors, and calculated evaporation duct heights using the four models, based on meteorological observations of the South China Sea, providing a theoretical basis and practical experience for future applications. In order to improve the applicability of the Babin model, Yu et al. (2015) performed a theoretical derivation of the model and conducted

simulations to analyze its sensitivity to input parameters. Based on atmospheric boundary layer theory, Liu et al. (2001) studied a theoretical formula for estimating the heights of evaporation ducts using similarity theory, with pseudo refractive index as the similarity parameter. Paulus (1985) applied the P-J model of evaporation ducts in operational and climatological assessments of propagation and examined the sensitivity of the model to meteorological measurements.

As discussed above, there have been many studies on diagnostic model calculations of heights of evaporation ducts over the ocean surface. The common models are the P-J model (Paulus, 1985), the Babin model (Babin et al., 1997), and the Naval Postgraduate School (NPS) model (Babin and Dockery, 2002). In addition, Sheng and Huang (2009, 2010) used radar echo to reverse the height of evaporation ducts. At present, traditional auto-regressive (AR) algorithms are mainly used to predict the heights of evaporation ducts (He et al., 2018). However, with the development of artificial intelligence in recent years, machine learning is being used more and more in meteorological prediction (Tag and Peak, 1996; Bankert et al., 2002; Wang et al., 2010; Lee et al., 2014; Rhee and Im, 2017; Czernecki et al., 2018). For example, Wang et al. (2010) predicted wind speeds using SVR. Xue et al. (2009) introduced the theory of the SVR, and developed an optimal meteorological prediction model based on SVR with genetic algorithms. Ham et al. (2019) showed that a statistical forecast model employing a deep-learning approach produces skillful El Niño-Southern Oscillation (ENSO) forecasts for lead times of up to one and a half years. Ebtehaj and Bonakdari (2016) proposed a novel method based on a combination of SVR and the firefly algorithm (FFA) to predict the minimum velocity required to avoid sediment settling in pipe channels. Besides, some new optimization algorithms can be seen from Wang et al. (2019), Zhao et al. (2019), and Chang et al. (2020). However, little research has so far been carried out on the prediction of evaporation duct heights using machine learning, so this is a key theme for the ongoing study of evaporation ducts. The traditional prediction method is AR method, which is a linear method. So this paper attempts to use SVR which is a non-linear method to predict evaporation duct heights. After that, we use the simulated annealing operator to improve SVR and apply it to the prediction of evaporation duct heights. Finally, the three prediction results are compared and analyzed to determine which is the best.

In this paper, a new diagnostic model of evaporation duct height, the Liuli 2.0 model, is proposed. High-resolution global positioning system (GPS) sounding data (He et al., 2020) and sea surface temperature (SST) data from the DMSP satellite from 2008 to 2009 over Hawaii are selected as the observational dataset. Based on the new model, the heights of evaporation ducts near the station at Coordinated Universal Time (UTC) = 12:00 are diagnosed on each day. Taking the diagnosed heights of evaporation ducts as a time series, and using the SVR algorithm improved by the simulated annealing operator, the first three quarters of the time series which has 549 samples is selected as training data. For each time step, three consecutive time steps are taken as input and the next time step as the output predicted evaporation duct heights. The last quarter of the time

series which has 182 samples is then used as the test sample, using RMSE and MAPE to evaluate the prediction by comparing the predicted value with the real value. Finally, the prediction results of the improved SVR algorithm are compared with those of a traditional AR algorithm and classical SVR algorithm to identify the advantages and disadvantages of the improved SVR algorithm. The new diagnosis and prediction method will provide a new method for studying the evaporation duct heights, which has certain reference significance for the study of the evaporation ducts.

ATMOSPHERIC DUCT DATA

Atmospheric Duct Definitions

Atmospheric refraction in radio meteorology refers to the bending of electromagnetic waves propagating in atmospheric media. The degree of refraction can be measured by the refractive index n (Kang et al., 2014), which is defined as the ratio of the propagation velocity c (speed of light) of a radio wave in free space to the propagation velocity v in the medium, as follows:

$$n = \frac{c}{v} \tag{1}$$

The normal value of the atmospheric refractive index at the Earth's surface is generally $1.00025-1.0004$ (Kang et al., 2014). Because of the small departure from unity, n is not convenient for practical application in the study of radio wave propagation. Therefore, the refractivity N of the atmosphere is defined (Kang et al., 2014) as follows:

$$N = \frac{77.6}{T} \times \left(p + \frac{4810e}{T} \right), \tag{2}$$

where p is the atmospheric pressure (hPa), T is the atmospheric thermodynamic temperature (K), and e is the vapor pressure (hPa). The atmospheric refractivity N near the surface generally varies between 250 and 400 (Kang et al., 2014). As the atmospheric pressure and water vapor decrease rapidly with increasing altitude, while the temperature decreases slowly, the atmospheric refractive index or refraction generally decreases with increasing height (Kang et al., 2014). When the distance of the propagation of the electromagnetic waves is short, the surface of the Earth can be approximated as a plane, but when this distance is long the curvature of the Earth must be considered. Treating the surface of the Earth as a plane means that the atmospheric refractivity gradient and its effect on the propagation of the electromagnetic waves can be evaluated more easily; in this case the atmospheric corrected refractivity M (Kang et al., 2014) is defined as follows:

$$M = N + 0.157Z = 77.6\frac{p}{T} + 3.73 \times 10^5 \times \frac{e}{T^2} + 0.157Z \tag{3}$$

where M is a dimensionless number. For statistical convenience, M is used as the variable under consideration. p, T, e, and Z are the atmospheric pressure (hPa), temperature (K), vapor
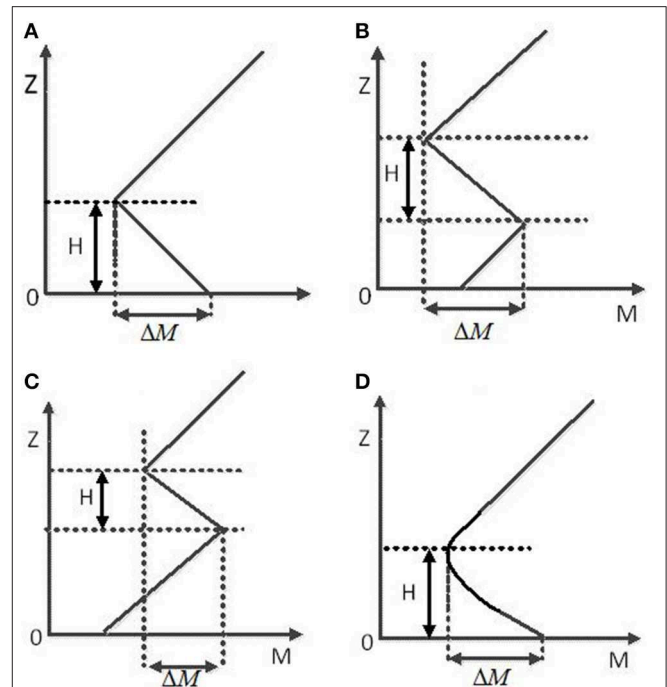
FIGURE 1 | Atmospheric duct definitions: **(A)** surface duct; **(B)** surface-based duct; **(C)** elevated duct; **(D)** evaporation duct. **(A–C)** usually appears over land. The difference between **(B)** and **(C)** is that the atmospheric corrected refractivity M at the second inflection point of **(B)** is smaller than that at the ground, while **(C)** is larger than that at the ground. **(D)** usually appears over the ocean and its height h does not exceed 40 m.

pressure (hPa), and height above ground (m), respectively. The lowest height at which the atmospheric corrected refractivity M satisfies $\frac{dM}{dz} < 0$ is defined as the bottom of the atmospheric duct layer. Above this, the lowest height at which $\frac{dM}{dz} > 0$ is defined as the top of the atmospheric duct layer (Kang et al., 2014). The difference between these two heights is defined as the thickness of the atmospheric duct and is represented by H. The difference in atmospheric corrected refractivity M between the bottom and the top of the atmospheric duct layer is defined as the intensity of the atmospheric duct, represented by ΔM. According to the changes in M with height, atmospheric ducts are primarily divided into four categories: surface ducts, surface-based ducts, elevated ducts, and evaporation ducts; as illustrated in **Figure 1**.

Preprocessing of Atmospheric Duct Data

The meteorological data used in this paper are high-resolution radiosonde data from the global telecommunication system and inversion data from the DMSP satellite. The data location is an observation station in Hawaii (U.S. state), with longitude and latitude (155.1°W, 19.7°N). Data are taken daily at UTC = 12:00 from 2008 to 2009. The high-resolution sounding data include meteorological parameters such as temperature, pressure, humidity, and wind at the height of the sounding balloon. The vertical resolution is 10–80 m below 100 m and 30–300 m at

100–1,000 m, and the typical thicknesses of atmospheric ducts are between tens of meters and hundreds of meters, so these sounding data are appropriate for studying atmospheric ducts. The SST data from the DMSP satellite were provided by NOAA, with a spatial resolution of $0.25° \times 0.25°$ and a temporal resolution of 3 h. The selected ocean area is about 1,000 m away from the station. First, the temperature, pressure, relative humidity, and wind speed at a height of 10 m are extracted from the high-resolution sounding data for each day. Then these data and the corresponding SSTs are put into the new height diagnostic model to diagnose the heights of evaporation ducts at this time. Finally, all calculation results are recorded as a time series X and the three points smoothing is then used to carry out low-pass filtering to get a new series X′. Specific methods are listed in section Preprocessing of Input Data. The series X′ obtained after smoothing is used for analysis and prediction by the traditional AR algorithm and the SVR algorithm improved by the simulated annealing operator. Considering the rapid change of the weather at sea, the influence of the ocean environment, measurement error, and turbulence, it is necessary to preprocess the meteorological data before using the new Liuli 2.0 model. Firstly, abnormal data are eliminated: specifically, the mean square deviation σ of the meteorological data is calculated, any data where the absolute difference between the data value and the average value is greater than 3σ are marked as an "abnormal value" and removed, and they are replaced using interpolation.

A NEW DIAGNOSTIC MODEL FOR EVAPORATION DUCT HEIGHTS: THE LIULI 2.0 MODEL

Introduction to the Liuli 2.0 Model

In the Liuli 2.0 model, the input parameters are atmospheric temperature, relative humidity, wind speed and pressure at a certain height, and SST. The height of the evaporation duct is obtained by introducing the K-theory flux observation method into the atmospheric refractive index equation. The difference between this model and the traditional model is that this model avoids the previous method of setting an initial value for the iterative calculation to determine the M-O length L and the characteristic parameters u_*, θ_*, and q_*, and instead selects a variable $\xi = \frac{z}{L}$ through the size of the overall Richardson number R_{ib}, then uses the size of ξ to determine these characteristic parameters, which can improve the stability and efficiency of the calculation.

Flux Algorithm Calculation Scheme

At present, most flux calculation schemes need to be iterative and have low accuracy (Fairall et al., 2003). The non-iterative scheme adopted by the Liuli 2.0 model is similar to the classical iterative method. It uses multiple regression, which makes the calculation scheme applicable to a wide roughness range. The parameterization scheme depends on the atmospheric stratification. Under stable

TABLE 1 | The eight categories divided according to the values of z/z_0 and z/z_{0t}.

Category	z/z_0	z/z_{0t}
1	10–160	0.607–100
2	160–10^5	0.607–100
3	10–80	100–10^7
4	80–10^5	100–10^7
5	10–40	10^7-10^{11}
6	40–10^5	10^7-10^{11}
7	10–40	10^{11}-1.07×10^{13}
8	40–10^5	10^{11}-1.07×10^{13}

conditions, the scheme is divided into eight different categories according to the values of z/z_0 and z/z_{0t}, Where z_0 is aerodynamic roughness length and z_{0t} is thermodynamic roughness height (Li et al., 2014), as shown in **Table 1**.

Then R_{ibcp} is calculated according to the category corresponding to the values of z/z_0 and z/z_{0t}:

$$R_{ibcp} = \sum C_{mn} \log(L_{OM})^m (L_{OH} - L_{OM})^n, \quad (4)$$

$$L_{Oi} = \log(z/z_{0i}). \quad (5)$$

Values of R_{ibcp} and C_{mn} for all categories are given in Li et al. (2014), and the parameters corresponding to the first category are shown in **Table 2** as an example.

According to the value of R_{ibcp}, we can determine the location of R_{ib}: for example, when the size of R_{ib} is between R_{ibcp1} and R_{ibcp2} it is section Introduction, when it is between R_{ibcp2} and R_{ibcp3} it is in section Atmospheric Duct Data, and so on. Finally, the following equation is used to calculate ξ:

$$\xi = R_{ib} \sum C_{ijk} R_{ib}^i L_{OM}^j (L_{OH} - L_{OM})^k, \quad (6)$$

$$R_{ib} = \frac{gz\Delta\theta}{\theta u^2}. \quad (7)$$

The coefficients C_{ijk} are given for the first category as an example, in **Table 3**.

Under unstable conditions, the scheme is divided into eight categories according to the values of R_{ib}, z/z_0, and z/z_{0t}, as shown in **Table 4**.

The value of ξ is calculated according to the category as follows:

$$\xi = R_{ib} \frac{L_{OM}^2}{L_{OH}} \sum C_{ijk} \left(\frac{-R_{ib}}{1 - R_{ib}}\right)^i L_{OM}^{-j} L_{OM}^{-k}. \quad (8)$$

The coefficients C_{ijk} have different values according to the calculation results of different iteration schemes. This paper uses

TABLE 2 | The coefficients of Equation (4).

Category		C_{00}	C_{10}	C_{20}	C_{01}	C_{11}	C_{21}	C_{02}	C_{12}
1	R_{ibc1}	0.3095	−0.2852	−0.2852	0.07955	−0.0161	0	0	−0.00011
	R_{ibc2}	0.3219	0.3219	0.2613	0.06753	−0.0310	0.00391	−0.0018	0.00117
	R_{ibc3}	0.3545	0.3545	−0.2569	0.06609	−0.0393	0.00564	−0.0034	0.00220
	R_{ibc4}	0.439	0.439	−0.3133	0.0893	−0.0711	0.01403	−0.0060	0.003981
	R_{ibc5}	0.6887	0.6887	−0.5375	0.1754	−0.1564	0.03489	−0.0128	0.00810
	R_{ibc6}	1.706	1.706	−1.62	0.5124	−0.5026	0.1239	−0.0358	0.02238

TABLE 3 | Coefficients of Equation (6) for category 1.

	Section 1	Section 2	Section 3	Section 4	Section 5	Section 6	Section 7
C_{000}	−1.134	0	0	0	0	0	0
C_{100}	31.1	86.35	−280.4	0	0	−17.32	−6.343
C_{200}	−71.16	0	3235	0	0	8.773	7.66
C_{300}	227.4	0	−6165	0	0	0	−0.7661
C_{001}	−0.2094	−11.53	−10.64	0	0	0	0.0125
C_{101}	3.293	194.9	193.8	0	1.113	0	−2.203
C_{201}	−20.11	−975.4	−1194	−12.37	−97.56	0	0.8896
C_{301}	14.42	1472	2161	0	159.4	0	−0.1273
C_{002}	0.1476	−2.535	−4.603	0	0	1.919	−0.00827
C_{102}	−0.07325	28.24	52.02	11.99	16.33	0	0.3327
C_{202}	0.5627	−61.13	−110.7	−15.63	−25.67	0.2679	−0.04613
C_{003}	−0.01178	−0.2378	−0.5367	−0.3157	−0.6447	−0.2892	0
C_{103}	0.0218	0.7405	1.503	0.2948	0.9718	0	−0.04968
C_{010}	1.405	13.6	30.26	0	6.821	10.27	7.513
C_{110}	−32.47	−316.2	−314.9	0	−57.13	0	0
C_{210}	46.59	1067	186	−108.1	227.3	0	−4.799
C_{310}	−38.25	−1494	0	317.8	−224	0	0.5598
C_{011}	−0.2286	8.023	9.038	0	0.9287	−3.457	−1.1612
C_{111}	−1.097	−91.31	−87.06	−12.52	−17.88	−1.617	0
C_{211}	−0.3394	213.7	198.6	0	34.41	0	0
C_{012}	0	1.035	1.529	0	0.319	−0.07536	0.4666
C_{112}	0	−5.072	−7.439	−1.025	−2.452	0	0.0605
C_{013}	0	0.03622	0.07369	0.4669	0.08583	0.05146	−0.01808
C_{020}	0	−4.699	−10.71	−1.896	−2.195	−3.108	0
C_{120}	10.71	97.46	122.1	28.39	22.21	7.948	2.442
C_{220}	0	−152.4	−76.91	−14.19	−31.44	−2.985	0.1584
C_{021}	0	−1.704	−2.035	0	−0.1355	0.8751	0
C_{121}	0	9.069	8.248	2.214	1.976	0.3139	−0.04377
C_{022}	0	−0.09576	−0.1263	−0.01472	−0.04636	−0.05131	−0.0694
C_{030}	−0.007485	0.4446	1.015	0.3069	0.1708	0.2598	−0.1675
C_{130}	−0.9671	−7.991	−10.96	−3.635	−1.623	−0.8513	−0.2181
C_{031}	0.003402	0.1138	0.1426	−0.008769	0	−0.05427	0.05052

C_{ijk} based on the results of the Paulson 70 scheme (Paulson, 1970), as shown in **Table 5** for category 1.

In the flux algorithm scheme, the turbulent flux τ and sensible heat flux H_s are defined as:

$$\tau = \rho u_*^2 = \rho C_m u^2, \qquad (9)$$
$$H_s = -\rho c_p u_* \theta_* = -\rho c_p C_h u(\theta - \theta_0). \qquad (10)$$

Here, ρ is the air density, c_p is the specific heat capacity at constant pressure, u_* is the characteristic wind speed, and θ_* is the characteristic temperature.

The overall transport coefficient of flux is defined as:

$$C_m = \frac{\kappa^2}{[\ln(\frac{z}{z_0}) - \psi_m(\xi) + \psi_m(\frac{z_0}{z}\xi) + \psi_m^*(\xi, \frac{z}{z_*})]^2} \qquad (11)$$

$$C_h = \frac{\kappa^2}{[\ln(\frac{z}{z_0}) - \psi_m(\xi) + \psi_m(\frac{z_0}{z}\xi) + \psi_m^*(\xi, \frac{z}{z_*})][\ln(\frac{z}{z_{0t}}) - \psi_h(\xi) + \psi_h(\frac{z_{0t}}{z}\xi) + \psi_h^*(\xi, \frac{z}{z_*})]} \tag{12}$$

$$\psi_h^*(\xi, \frac{z}{z_*}) = \varphi_{m,h}[(1 + \frac{\nu}{\mu z/z_*})\xi]\frac{1}{\lambda}(1 + \frac{\lambda}{\mu z/z_*})\exp(-\mu z/z_*). \tag{13}$$

Here, κ is the von-Karman constant, z_0 is the aerodynamic roughness height, z_{0t} is the thermodynamic roughness, z_{0q} is the water vapor roughness, and the coefficients $\lambda = 1.5, \mu = \mu_m = 2.59, \mu = \mu_h = 0.95$, and $\nu = 0.5$.

Under stable conditions, according to the CB05 flux scheme (Li et al., 2015), the stability correction function is defined as:

$$\begin{cases} \varphi_m = 1 + a\frac{\xi + \xi^b(1+\xi^b)^{\frac{1-b}{b}}}{\xi + (1+\xi^b)^{\frac{1}{b}}} \\ \varphi_h = 1 + c\frac{\xi + \xi^d(1+\xi^d)^{\frac{1-d}{d}}}{\xi + (1+\xi^d)^{\frac{1}{d}}} \end{cases}. \tag{14}$$

In Equation (14), $a = 6.1, b = 2.5, c = 5.3, d = 1.1$ and $\xi = \frac{z}{L}$.

Under unstable conditions, the stability correction function is defined as:

$$\begin{cases} \varphi_m = (1 - A_m\xi)^{-\frac{1}{4}} \\ \varphi_q = \varphi_h = \alpha(1 - A_h\xi)^{-\frac{1}{2}} \end{cases}. \tag{15}$$

In Equation (15), according to Paulson (1970), $\alpha = 16, A_h = 16$, and $A_m = 16$.

At the height of an evaporation duct, the following formula applies (Liu et al., 2017):

$$A + 0.157 = \frac{E\varphi_h}{kz\sqrt{-\frac{\tau}{\rho}}}H_s + \frac{F\varphi_q}{kz\sqrt{-\frac{\tau}{\rho}}}H_l. \tag{16}$$

The following formula is used to determine φ_h and φ_q in this paper:

$$\varphi_h = \varphi_q = \begin{cases} 1 + c\frac{\xi + \xi^d(1+\xi^d)^{\frac{1-d}{d}}}{(1+\xi^d)^{\frac{1}{d}}} & (\frac{z}{L} \geq 0) \\ (1 - 16\frac{z}{L})^{-\frac{1}{2}} & (\frac{z}{L} < 0) \end{cases}. \tag{17}$$

TABLE 4 | The eight categories divided according to the values of R_{ib}, z/z_0 and z/z_{0t}.

Region	R_{ib}	z/z_0	z/z_{0t}
1		$10 \leq z/z_0 \leq 80$	$0.607 \leq z/z_{0t} \leq 10$
2		$10 \leq z/z_0 \leq 80$	$10 < z/z_{0t} \leq 1.069 \times 10^{13}$
3		$80 < z/z_0 \leq 10^5$	$0.607 \leq z/z_{0t} \leq 10$
4		$80 < z/z_0 \leq 10^5$	$10 < z/z_{0t} \leq 1.069 \times 10^{13}$
5	$-5 < R_{ib} < -2$	$10 \leq z/z_0 \leq 80$	$0.607 \leq z/z_{0t} \leq 10$
6	$-5 < R_{ib} < -2$	$10 \leq z/z_0 \leq 80$	$10 < z/z_{0t} \leq 1.069 \times 10^{13}$
7	$-5 < R_{ib} < -2$	$80 < z/z_0 \leq 10^5$	$0.607 \leq z/z_{0t} \leq 10$
8	$-5 < R_{ib} < -2$	$80 < z/z_0 \leq 10^5$	$10 < z/z_{0t} \leq 1.069 \times 10^{13}$

Under neutral conditions $(\frac{z}{L}=0)$, the evaporation duct height is therefore given by:

$$Z_{EDH} = \frac{1}{k(A + 0.157)}\sqrt{-\frac{\rho}{\tau}}(EH_s + FH_l); \tag{18}$$

under stable conditions, the evaporation duct height is given by:

$$Z_{EDH} = \frac{(EH_s + FH_l)(1 + 5.3 \times \frac{\frac{z_{EDH}}{L} + \frac{z_{EDH}}{L}^{1.1}(1+\frac{z_{EDH}}{L}^{1.1})^{-\frac{1}{11}}}{\frac{z_{EDH}}{L} + (1+\frac{z_{EDH}}{L}^{1.1})^{\frac{1}{1.1}}})}{k(A + 0.157)\sqrt{-\frac{\tau}{\rho}}}. \tag{19}$$

and under unstable conditions, the evaporation duct height is given by:

$$z_{EDH}\sqrt{1 - 16\frac{z_{EDH}}{L}} = \frac{EH_s + FH_l}{k(A + 0.157)\sqrt{-\frac{\tau}{\rho}}}. \tag{20}$$

Equations (18)–(20) can be used to calculate the heights of evaporation ducts under different atmospheric stratification conditions by selecting the appropriate iterative method.

Putting the meteorological data from the selected station into the model, the calculation results are shown in **Figure 2**. It can be seen from this that the evaporation duct heights form a stationary time series, which is roughly consistent with the height distribution of the evaporation ducts calculated by Babin et al. (1997) and Paulus (1985).

PREDICTION METHOD

Traditional AR Prediction Algorithm
Overview of AR

The auto-regressive (AR) algorithm is a time series processing method developed from linear regression analysis (Twiddle et al., 2006). The method uses itself as the regression variable, i.e., a linear combination of random variables in an earlier period is used to describe the linear regression process of random variables in a later period (Twiddle et al., 2006). Compared with other linear regression models, AR does not use x to predict y, but x to predict x. It is therefore widely used for prediction in economics, informatics, natural sciences, and other areas. Its basic principle is described in the following paragraph (see also Huang, 2004).

Suppose that a time series $\{X_t\}$ satisfies:

$$X_t = \varphi_0 + \varphi_1 X_{t-1} + \cdots + \varphi_p X_{t-p} + a_t, \tag{21}$$

TABLE 5 | Coefficients of Equation (8) for category 1.

	Region 1	Region 2	Region 3	Region 4	Region 5	Region 6	Region 7	Region 8
C_{031}	−28.813	0	0	0	0	0	0	0
C_{013}	0	0	0	0	0	0	0	0
C_{103}	0	0	0	0	0	0	0	0
C_{130}	0	0	0	0	0	0	0	0
C_{022}	171.37	21.868	0	0	71.863	0	0	0
C_{112}	0	0	0	0	0	0	0	0
C_{121}	0	0	0	98.068	0	0	0	0
C_{003}	−4.4659	−2193.5	0	0	0	−1490	0	0
C_{030}	0	0	0	0	−30.825	0	−333.57	0
C_{012}	−145.38	24.905	63.562	0	−26.723	−48.521	−625.04	−35.527
C_{021}	0	0	−133.56	0	0	0	914.04	0
C_{102}	−2.9284	6.6752	0	0	−11.479	0	0	0
C_{120}	11.867	0	0	0	−1.2311	0	0	0
C_{111}	−7.1901	1.9789	0	0	−67.415	2.8259	0	0
C_{002}	31.481	5.7057	0	4.5019	16.059	27.861	149.79	32.682
C_{020}	0	3.2231	34.817	5.4319	23.452	2.9699	83.588	10.73
C_{011}	19.158	−14.009	0	0	5.5104	−7.3367	−209.17	−19.373
C_{101}	7.1458	0	5.337	0.65443	20.643	0	1.7803	0
C_{110}	−7.8929	−1.2357	−4.8263	−1.6828	0	0	0	0
C_{001}	−6.2982	0	1.5325	−0.7537	−5.5493	−2.1701	0	0
C_{010}	0	0	−7.0107	−1.4565	−4.764	−1.0425	−4.9982	−3.344
C_{100}	0	−0.43163	−0.21693	−0.20131	−1.6828	−0.79024	−0.51948	−0.53418
C_{000}	1.1233	1.0384	1.2577	1.0603	1.6062	1.3643	1.4222	1.3386
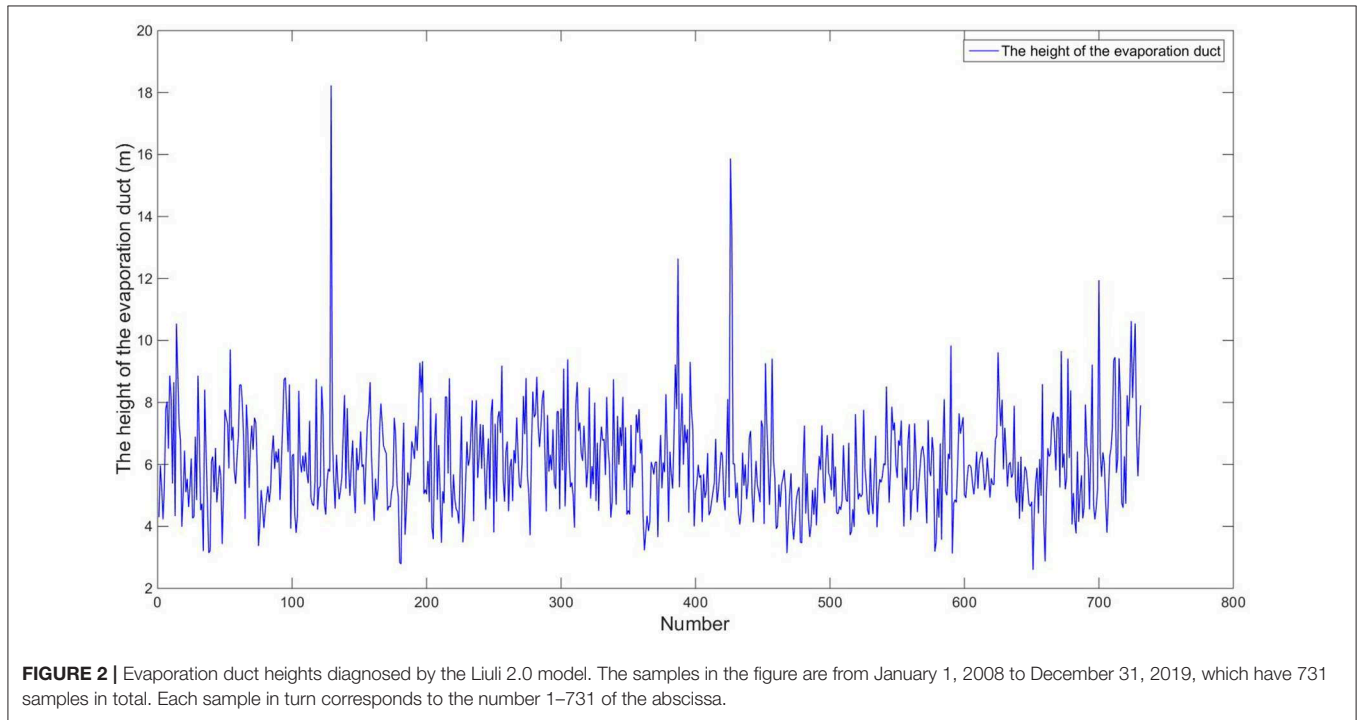
FIGURE 2 | Evaporation duct heights diagnosed by the Liuli 2.0 model. The samples in the figure are from January 1, 2008 to December 31, 2019, which have 731 samples in total. Each sample in turn corresponds to the number 1–731 of the abscissa.

where $\{a_t\}$ is a white noise sequence and $\varphi_0, \varphi_1, \cdots \varphi_p$ are real numbers. This algorithm is denoted as AR(p), and $\{X_t\}$ suitable for this algorithm is called the sequence of AR(p). The centralized algorithm of AR is used in this paper, that is, $\varphi_0 = 0$.

Generally, we can define the polynomial $\varphi(u) = 1 - \varphi_1 u - \cdots - \varphi_p u^p$ as the auto-regressive polynomial of an AR(p) algorithm. Letting $\partial(L) = 1 - \varphi_1 L - \varphi_2 L^2 - \cdots - \varphi_p L^p$, the operator expression of the AR(p) algorithm can be expressed as:

$$\partial(L)X_t = a_t. \tag{22}$$

From Equation (21), it can be concluded that:

$$(1 - \varphi_1 L - \varphi_2 L^2 - \cdots - \varphi_p L^p)X_t = a_t, \tag{23}$$

so the solution of the AR(p) algorithm is as follows:

$$X_t = \frac{1}{\varphi(L)} a_t = \sum_{j=0}^{\infty} \phi_j L^j a_t = \sum_{j=0}^{\infty} \phi_j a_{t-j}, \tag{24}$$

where $\phi_0 = 1$.

Establishment of the AR Algorithm
Preprocessing of input data
The evaporation duct height data calculated by the Liuli 2.0 model still contain a large amount of clutter, so it is necessary to carry out low-pass filtering to obtain a new sample sequence. The specific smoothing method is described in the following paragraph (see also Huang, 2004).

The 3-day smoothing average evaporation duct height is calculated on a 1-day time step as follows:

$$X'_n = \frac{\sum_{i=a}^{n} x_i}{m}, \tag{25}$$

where X'_n is the average evaporation duct height calculated at the nth time, x_i is the evaporation duct height value calculated at the ith time, and a is the first sample in the smoothing average range: when $n \leq N$, $a = 1$, and when $n > N$, $a = n - N + 1$; N is the total number of samples and n is the number of samples in the current smoothing average range. The result after smoothing is shown in **Figure 3**. The sample sequence X' obtained by smoothing is used for analysis and prediction by the traditional AR algorithm.

Choice of the order of the algorithm
In establishing an ideal algorithm AR(p), it is not possible to know in advance the appropriate order p. Different orders should be tested, so that the best order can be chosen for the final algorithm. Generally, the scheme used is a dynamic modeling scheme, which uses a series $AR(m), (m = 1, 2 \cdots)$ to approximate data step by step, and, at each step, the approximation effect is evaluated by the reduction in the sum of squares of residuals. If the sum of squared residuals does not improve significantly, the test of further increasing m is not carried out. Experiment shows that if m is increased not by 1 but by 2 every time, this is advantageous, and more computationally efficient. The specific methods are described in the following (see also Huang, 2004).

If AR(m) is the current model, the AR($m+1$) is the model to be tested. It is observed whether the reduction in the sum of the squares of the residuals exceeds a standard significance. This is carried out according to the following formula:

$$F = \frac{(A_1 - A_0)/s}{A_0/(n-r)}. \tag{26}$$

The variable F follows the F-distribution of the freedom degree of molecule s and denominator n-r. A_0 is the sum of squares of residuals of the model to be tested, A_1 is the sum of squares of the residuals of the previous model, r is the sum of two parameters of model A_0, and s is the difference of a parameter between model A_1 and model A_0. In changing from AR(m) to AR($m + 1$), if $F > F_{5\%}$, then the improvement in the sum of squares of the residuals is significant, implying that the AR(m) model is insufficient. If $F < F_{5\%}$, then AR(m) can be considered to be appropriate at this significance level. The results in **Table 6** were obtained for this paper. It can be seen that, when $m = 2$, the model passes the 95% significance test. Therefore, in this paper, the AR(2) model is selected for the time series prediction.

The SVR Prediction Algorithm Improved by the Simulated Annealing Operator
Overview of the SVR
The support vector machine is an important part of statistical learning theory, and also the most practically applicable part (Yuan et al., 2010). In pattern recognition, in order to find decision rules with generalization ability, some subsets of the selected training data are denoted as support vectors. The best separation of support vectors is equivalent to the separation of all data. Support vector machines are similar to neural networks; the output is a linear combination of intermediate nodes, and each intermediate node corresponds to a support vector. Its structure is shown in **Figure 4**. In recent years, support vector machines have also shown excellent performance in research on regression algorithms, so a new algorithm has been developed, the support vector regression (Basak et al., 2007), which has been successfully applied to the prediction of time series.

This paper uses the SVR, and the principle is described in the following (see also Basak et al., 2007):

For a given sample set $S = \{(x_1, y_1), ..., (x_l, y_l)| x_i \in R^n, y_i \in R\}$, where the vector x_i is the input sample of the model and y_i is the corresponding output sample, the regression problem is to find out the relationship between x_i and y_i:

$$y = f(x) = < w \cdot \varphi(x) > + b. \tag{27}$$

Here, $< \cdot >$ represents a mapping of the input samples in the original space to the inner product of the high-dimensional space using the kernel function, so that the non-linear problem in the original space can be transformed into a linear problem in the high-dimensional space. The insensitivity loss ε ($\varepsilon > 0$) is introduced, according to:

$$L = |y - f(x)| = \begin{cases} 0 & if |y - f(x)| \leq \varepsilon \\ |y - f(x)| - \varepsilon & otherwise. \end{cases} \tag{28}$$
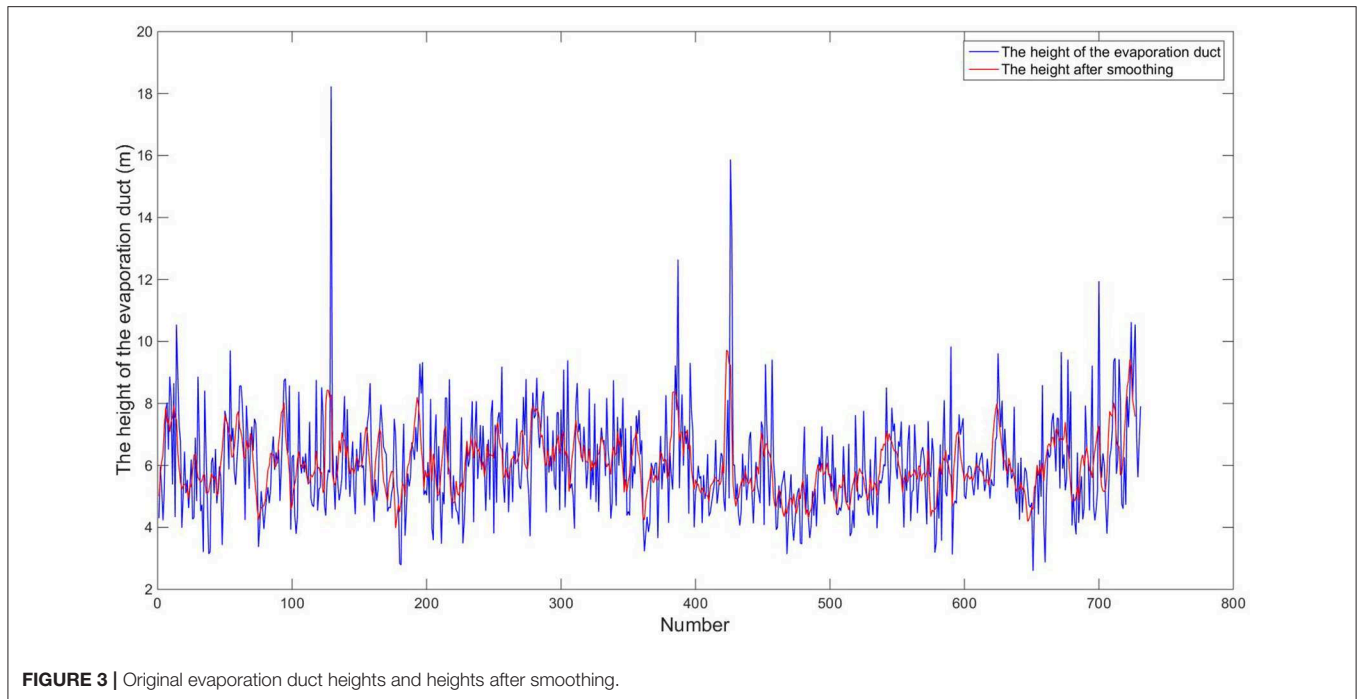
FIGURE 3 | Original evaporation duct heights and heights after smoothing.

TABLE 6 | Results of the F test.

	F	$F_{5\%}$
$m = 1$	7.24	3.90
$m = 2$	0.18	3.89

When the loss function satisfies this equation, the optimal solution is obtained. By introducing relaxation variables of ξ_i and ξ_i^*, the above problems can be transformed into optimization problems as follows:

$$\min\{\tfrac{1}{2}||w||^2 + C\sum_{i=1}^{l}(\xi_i + \xi_i^*), \xi_i, \xi_i^* \geq 0, C \geq 0\}.$$
$$s.t. |f(x) - y_i| \leq \varepsilon, i = 1, 2, 3, ..., l \tag{29}$$

Here, the first term improves the generalization ability, and the second item improves the accuracy. To solve these optimization problems, a Lagrangian function is constructed:

$$L(w, b, \xi, \xi^*, \alpha, \alpha^*) = \frac{1}{2}||w||^2 + C\sum_{i=1}^{l}(\xi + \xi^*)$$
$$- \sum_{i=1}^{l}\alpha_i[\xi_i + \varepsilon - y_i + f(x)]$$
$$+ \sum_{i=1}^{l}\alpha_i^*[\xi_i + \varepsilon + y_i - f(x)] \tag{30}$$

where $\alpha_i, \alpha_i^* \geq 0; i = 1, ..., l$.
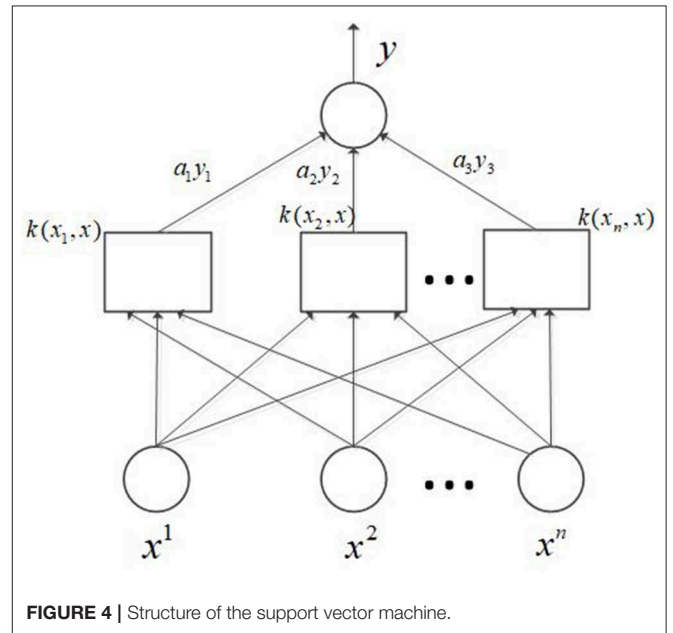
FIGURE 4 | Structure of the support vector machine.

In Equation (30), the partial derivatives with respect to w, b, ξ_i, and ξ_i^* are calculated as follows:

$$\frac{\partial}{\partial w}L = 0, \frac{\partial}{\partial b}L = 0, \frac{\partial}{\partial \xi_i}L = 0, \frac{\partial}{\partial \xi_i^*}L = 0. \tag{31}$$

After simplifying Equation (31), we obtain:

$$\sum_{i=1}^{l} (\alpha_i - \alpha_i^*) = 0, w = \sum_{i=1}^{l} (\alpha_i - \alpha_i^*)\varphi(x_i)$$
$$C - \alpha_i = 0, C - \alpha_i^* = 0, i = 1, ..., l. \tag{32}$$

In Equation (32), sample data for which $\alpha_i - \alpha_i^*$ is not equal to zero represent the support vector. The dual form of the non-linear optimization problem can be obtained from Equation (32), so the regression function can be rewritten as:

$$f(x) = \sum_{i=1}^{l} (\alpha_i - \alpha_i^*)K(x_i, x) + b, x_i \in R^n, b \in R. \tag{33}$$

Therefore, using existing input and output samples, the output expression is obtained through the training of the SVR, and then, using Equation (33), the output data of a new sample can be obtained by inputting data from this sample, so as to achieve the data prediction.

Establishment of the Improved SVR Algorithm

Preprocessing of input data
Similarly to the auto-regressive algorithm, the improved SVR algorithm needs to preprocess the data before they are input. The method is the same as for the auto-regressive algorithm, so it will not be repeated here.

Normalization of data
In order to prevent output saturation caused by large absolute input values, the training sample is normalized before it is input to the input layer of the SVR, so that the data vector falls within the range [0,1] or [−1,1]; it also needs to be denormalized when the SVR outputs the data. The normalization means that input and output vector data have similar weights in each dimension and prevents one dimension from dominating the weighting algorithm. The normalization formula is as follows:

$$x_i' = \frac{x_i - x_{min}}{x_{max} - x_{min}}, \tag{34}$$

where x_i is the input or output data, x_{min} is the minimum value in the dataset, and x_{max} is the maximum value in the dataset.

Selection of algorithm parameters
The selection process for the improved SVR algorithm includes the choice of kernel function and the optimization of parameters.

Selection of kernel function. There are mainly three kinds of kernel functions: linear kernel function, polynomial kernel function, and radial basis kernel function. The linear kernel function is not suitable for this algorithm, because the SVR is non-linear. The polynomial kernel function has many super-parameters, which makes its structure complex. In addition, polynomial kernel function is suitable for orthogonal normalized data, so it is also not suitable for this algorithm. The radial basis function (RBF) kernel is a kind of kernel function with strong locality, which can map a sample to a higher dimensional space for both large and small samples, and it has better anti-interference ability for the noise in the data. Besides, it has only one super-parameter σ, so this is chosen for this paper. The expression is as follows:

$$K(x_i, x_j) = \exp\left(-\frac{||x_i - x_j||^2}{2\sigma^2}\right). \tag{35}$$

Selection of parameters. The main parameters to be selected in the prediction model are the penalty parameter C, the insensitivity loss degree ε, and kernel function parameter σ. To select these three parameters, we use the simulated annealing operator (Serrurier and Prade, 2008) to find the optimal values. The simulated annealing operator starts from a certain state and adjusts the current state according to the current temperature to generate a new state (Serrurier and Prade, 2008). It has five adjustable parameters: the starting temperature T (T $= 1 \times 10^7$), the ending temperature T_{min} ($T_{min} = 1 \times 10^{-6}$), temperature decreasing rate C_1 ($C_1 = 0.99$), the maximum number of iterations N (N $= 1 \times 10^8$), and the minimum boundary value of each parameter n (n $= 1 \times 10^{-8}$). If the new state is better, the new state is accepted. If the new state is worse, a probability will be generated based on the current temperature and the difference between the results of the two states. The system then decides whether to accept the state according to this probability. After each state transition, the temperature value is reduced, and the search stops the temperature value goes below a predetermined minimum value.

In this paper, the state is determined by three variables, the penalty parameter C, insensitivity loss ε, and kernel function parameter σ. The vector X_i composed of these three variables is taken as a state, and the RMSE of the regression prediction algorithm obtained for this state is taken as the evaluation function $f(X_i)$. The specific steps are illustrated in **Figure 5**, and are described as follows:

(1) Set the initial state X_i, temperature T and minimum temperature T_{min}

(2) Move to the next state X'_i based on the current state

(3) If $f(X_i) > f(X'_i)$, accept the status and go to (5)

(4) Generate the probability $P = e^{\frac{-(f(X')-f(X))}{T}}$, and generate a random number p between 0 and 1. If $p < P$, the system accepts the state, otherwise it does not.

(5) Calculate T= T * 0.99, if the current value of $f(X')$ is the optimal value, the new optimal state is retained.

(6) If T $< T_{min}$, the algorithm ends, otherwise go to (2).

After applying the above algorithm, the optimal parameters found were: C=187511.19, ε=0.00181, and σ=0.001812.

DISCUSSION AND ANALYSIS OF RESULTS

The total number of sample X' is 731, after the algorithm is completed, the first 549 samples are used as training sets, and
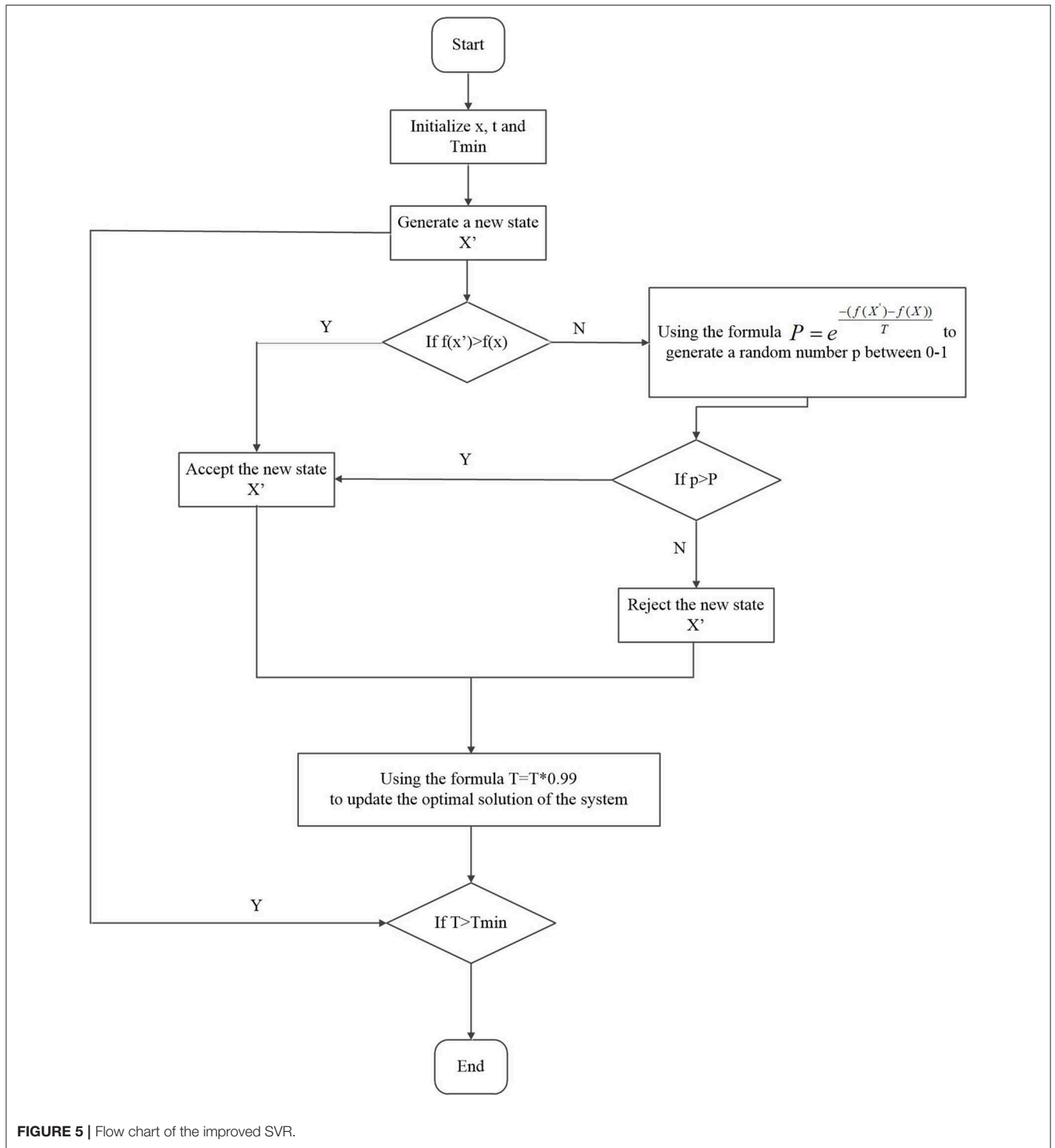
FIGURE 5 | Flow chart of the improved SVR.

the last 182 samples are used as test sets to verify whether the predicted results are similar to the actual values. **Figures 6–8** show comparisons between predicted values using the three algorithms, and real values, for the last 182 samples of time series X'.

From **Figures 6–8**, we can see that the prediction curves of the three algorithms follow the same trends as the true values.

In order to evaluate the quality of prediction, we use RMSE and MAPE, which are calculated as follows:

$$RMSE = \sqrt{\frac{\sum\limits_{i=1}^{N} (X_{obs,i} - X_{\text{mod }el,i})^2}{N}} \qquad (36)$$
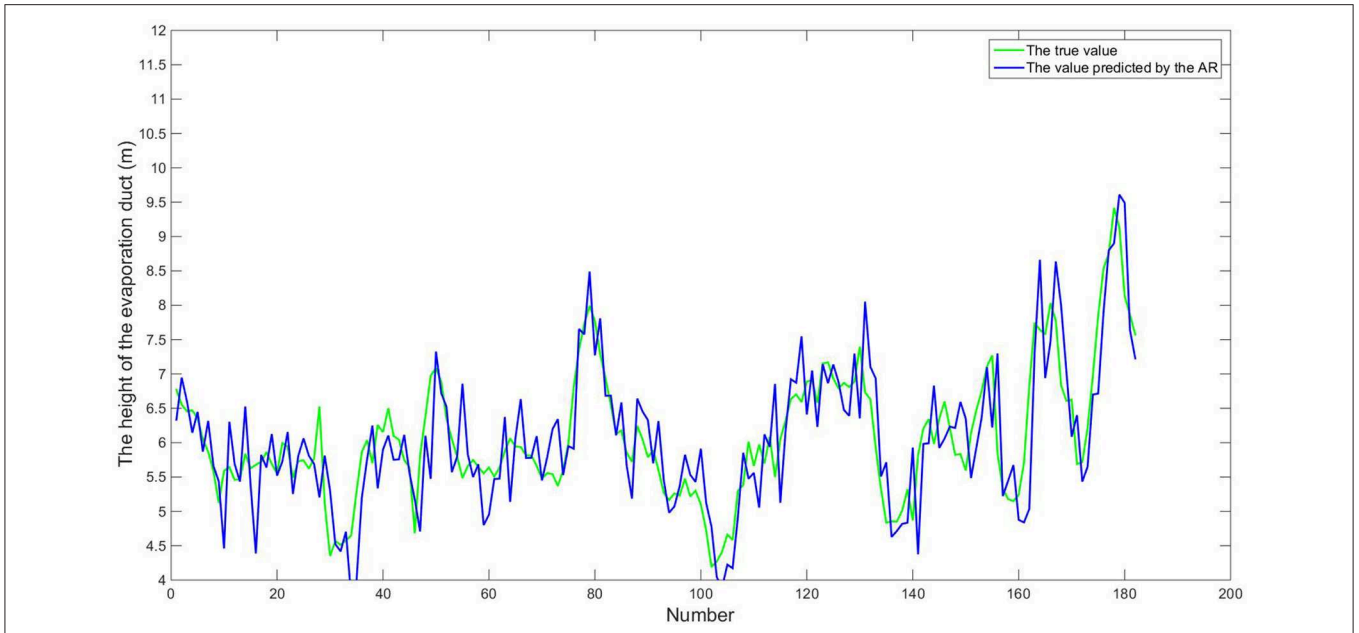
FIGURE 6 | Real values and values predicted by AR algorithm. The samples in the figure are from July 3, 2008 to December 31, 2019, which have 182 samples in total. Each sample in turn corresponds to the number 1–182 of the abscissa.
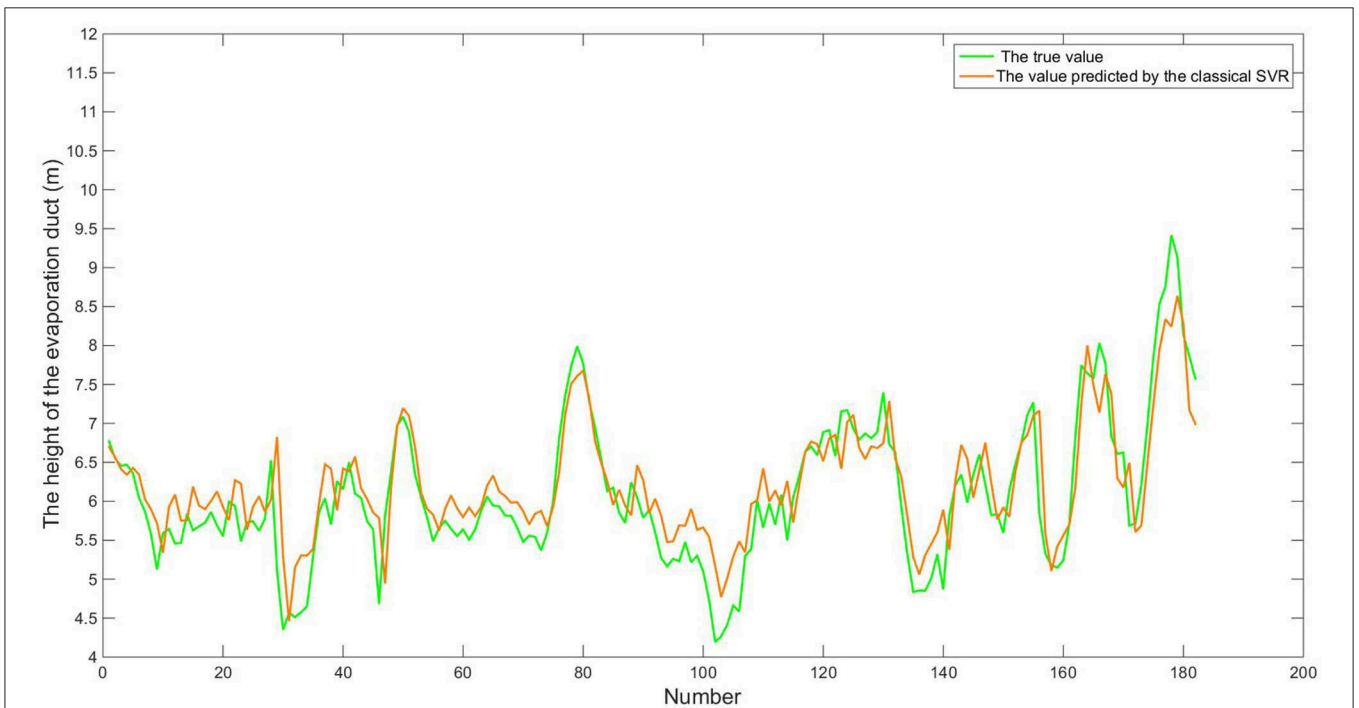
FIGURE 7 | Real values and values predicted by classical SVR algorithm. The samples in the figure are from July 3, 2008 to December 31, 2019, which have 182 samples in total. Each sample in turn corresponds to the number 1–182 of the abscissa.

$$MAPE = \frac{1}{N} \sum_{i=1}^{N} \frac{\left| X_{obs,i} - X_{\mathrm{mod}\,el,i} \right|}{X_{obs,i}} \times 100\%. \qquad (37)$$

Figures 9, **10** show the individual RMSEs and MAPEs of the last quarter of time series X', using the three prediction algorithms. **Table 7** shows the corresponding overall RMSE and MAPE values.
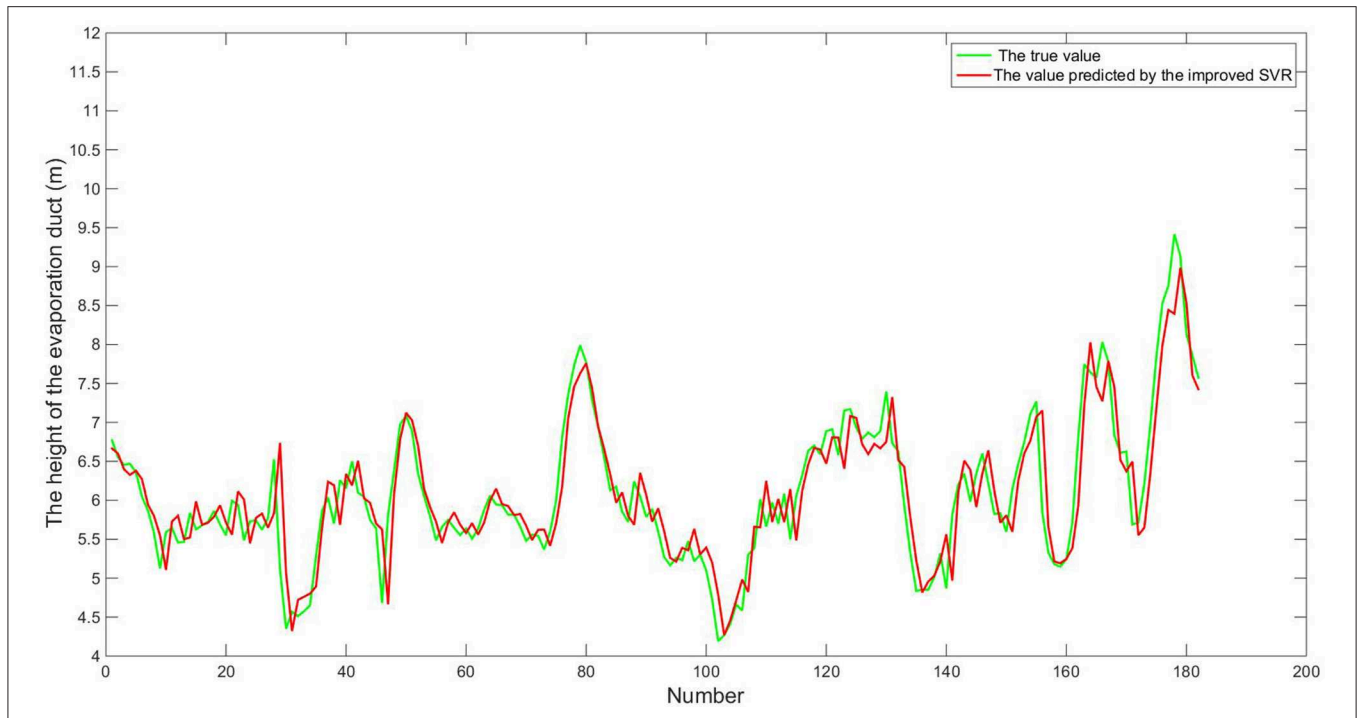
FIGURE 8 | Real values and values predicted by improved SVR algorithm. The samples in the figure are from July 3, 2008 to December 31, 2019, which have 182 samples in total. Each sample in turn corresponds to the number 1–182 of the abscissa.
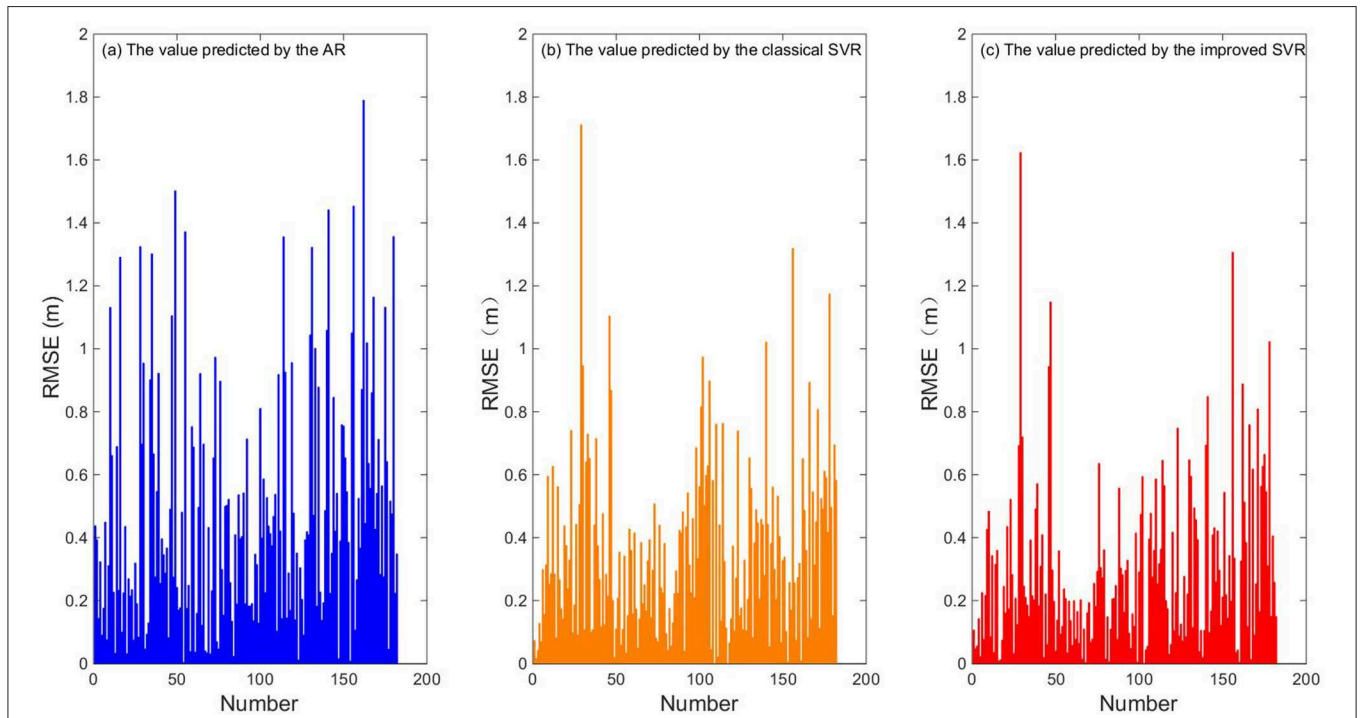
FIGURE 9 | RMSE of evaporation duct heights.

From **Figures 9**, **10**, we can see that nearly one-third of the RMSE values using the traditional AR algorithm are more than 0.5, and nearly one-third of the MAPE values are more than 10%, and nearly one-fourth of the RMSE values using the classical SVR algorithm are more than 0.5, and nearly one-fourth of the MAPE values are more than 10%, whereas most of the
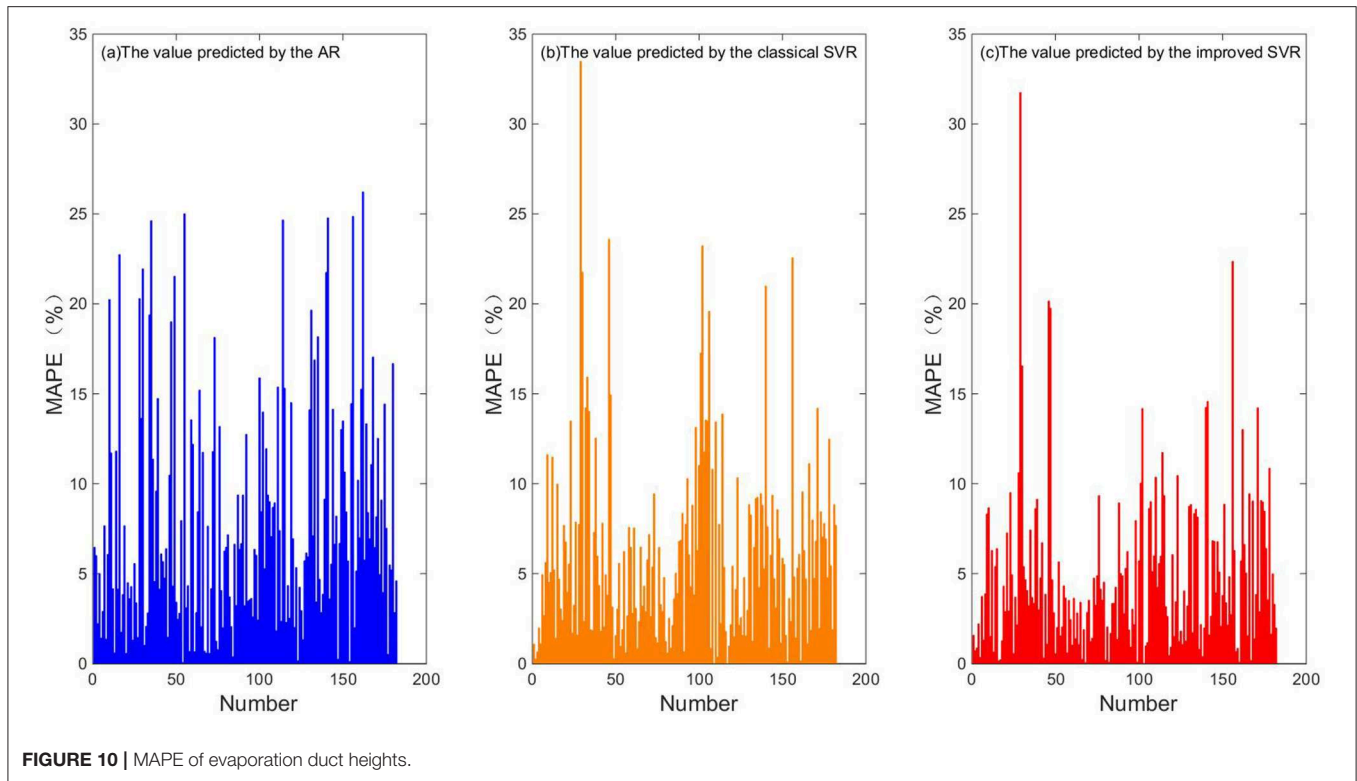
FIGURE 10 | MAPE of evaporation duct heights.

TABLE 7 | Analysis of overall error.

	RMSE (m)	MAPE (%)
AR	0.60	7.79
Traditional SVR	0.45	5.66
Improved SVR	0.38	4.78

RMSE values using the improved SVR algorithm are less than 0.5, and most of the MAPE values are less than 10%. From **Table 7**, we can see that the overall RMSE using the traditional AR algorithm is 0.60, and the MAPE is 7.79%, and the overall RMSE using the classical SVR algorithm is 0.45, and the MAPE is 6.10%, while the overall RMSE using the improved SVR algorithm is 0.38, and the MAPE is 4.78%. The prediction error of improved SVR algorithm is about 37% lower than that of the traditional AR algorithm and 15% lower than that of the classical SVR algorithm. **Figures 11–13** are the fitting graphs obtained by univariate linear regression (Neto et al., 2004) of the real and predicted values of the last 182 samples of the time series.

From **Figures 11–13**, we can see that the correlation coefficient r of the traditional AR algorithm is 0.8186, and the sum of squares of residuals is $R^2 = 63.8501$, and the correlation coefficient r of the classical algorithm is 0.8990, and the sum of squares of residuals is $R^2 = 22.9994$, while the correlation coefficient r of the improved SVR algorithm is 0.9097, and the sum of squares of

residuals is $R^2 = 21.566$. The prediction accuracy of the improved SVR algorithm is the highest, so its correlation coefficient r is the largest, and its residual adjustment and R^2 is the smallest, which shows that it has a better performance overall.

CONCLUSION AND FUTURE WORK

In this paper, a new diagnostic model of evaporation duct heights, the Liuli 2.0 model, is proposed. The difference between this model and the traditional model is that, when determining the M-O length L and the characteristic parameters u_*, θ_*, and q_*, it avoids the previous method of setting an initial value for an iterative calculation to determine these parameters, but instead selects a variable $\xi = \frac{z}{L}$, through the size of the overall Richardson number R_{ib}, then uses the size of ξ to determine the characteristic parameters. This can improve the stability and efficiency of the calculation, saving a large amount of computation time. Using high-resolution sounding data and retrieved SST data from the DMSP satellite from 2008 to 2009 at a Hawaiian station, the height of the evaporation ducts near the station is diagnosed according to the model. Then, the traditional AR algorithm, classical SVR algorithm and the SVR algorithm improved by a simulated annealing operator, are used to analyze and predict time series of evaporation duct heights, and the prediction results are compared to verify the advantages and disadvantages of the improved SVR algorithm. The results show that the prediction error of the improved SVR algorithm
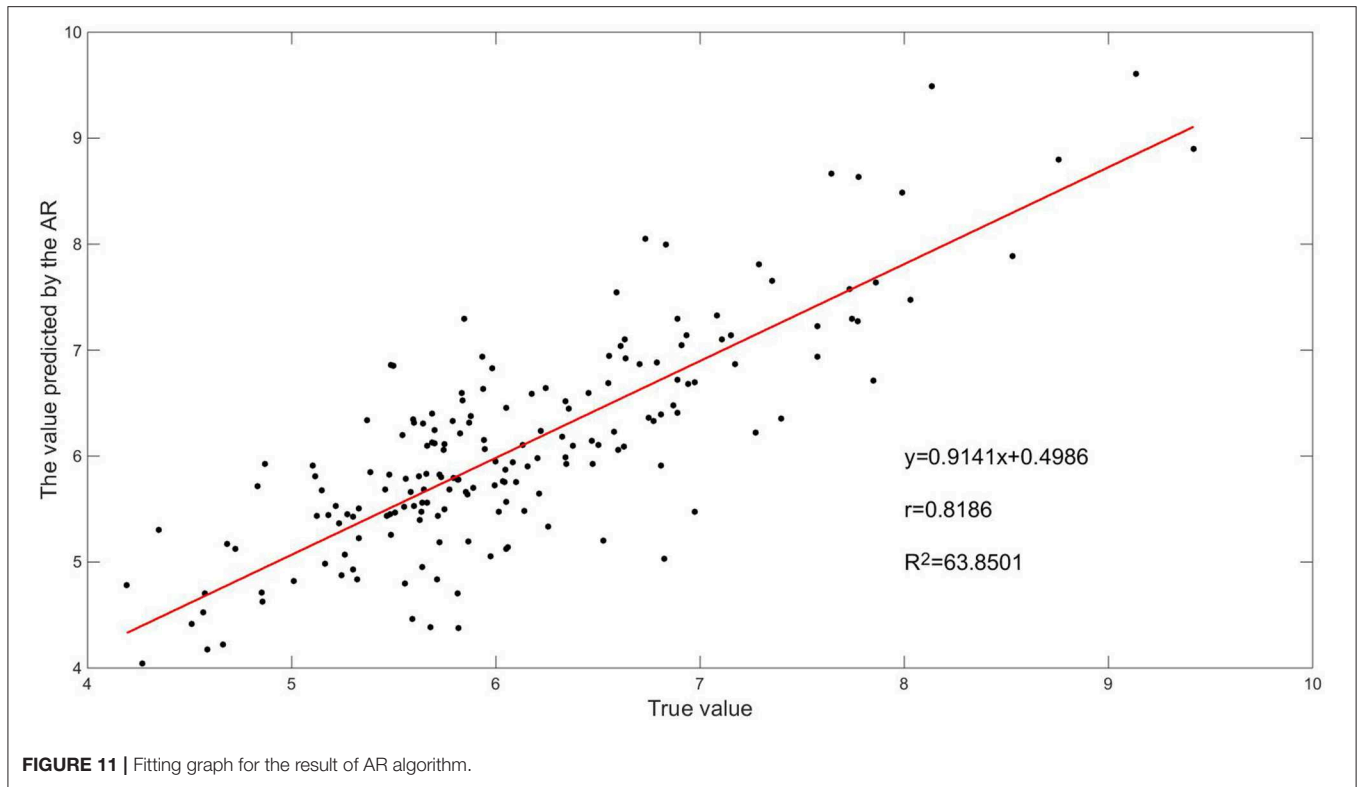
FIGURE 11 | Fitting graph for the result of AR algorithm.

$y=0.9141x+0.4986$

$r=0.8186$

$R^2=63.8501$
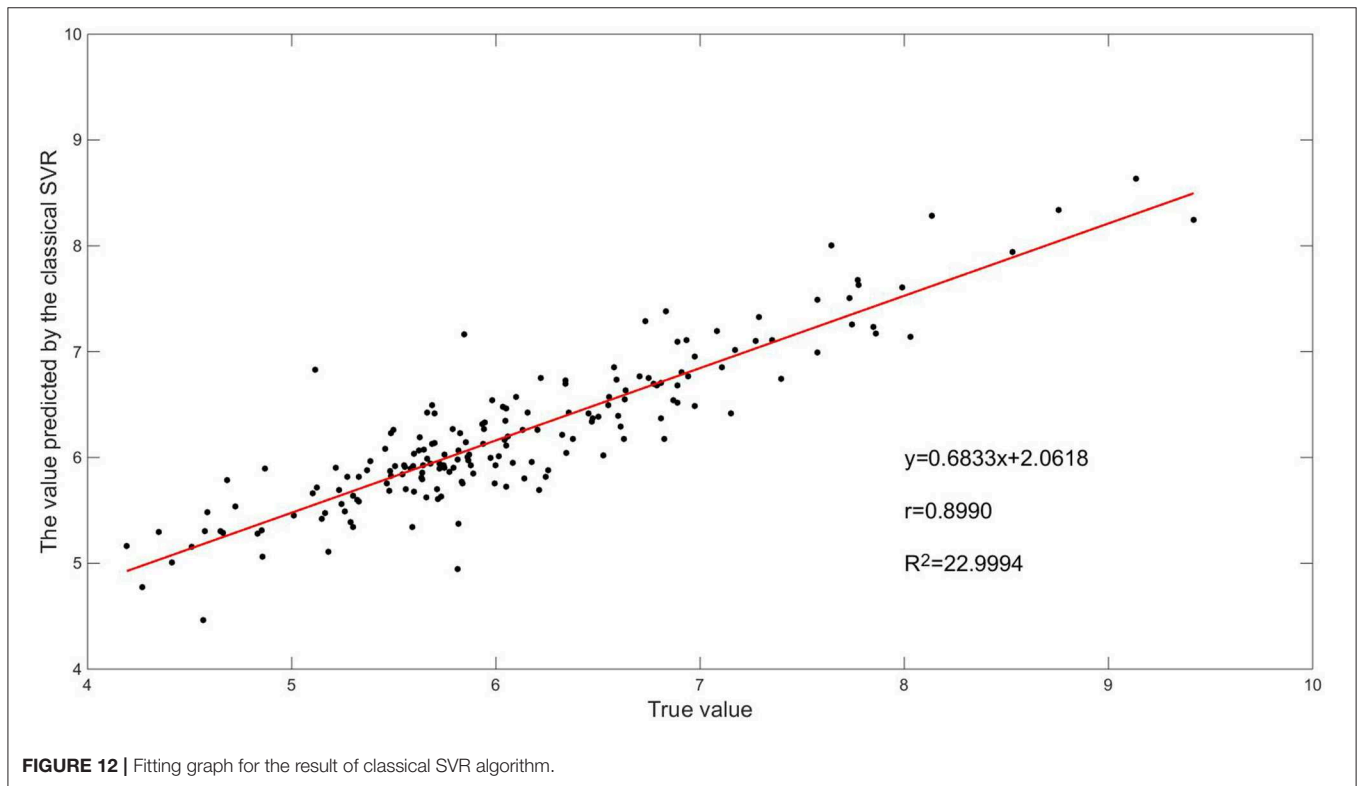
FIGURE 12 | Fitting graph for the result of classical SVR algorithm.

$y=0.6833x+2.0618$

$r=0.8990$

$R^2=22.9994$

is 37% lower than that of the traditional AR algorithm and 15% lower than that of the classical SVR algorithm. It has a good accuracy and strong generalization ability, and acts as a

reference for the study of short-term prediction of evaporation duct heights. The new diagnosis and prediction method will provide a new method for studying the evaporation duct heights,
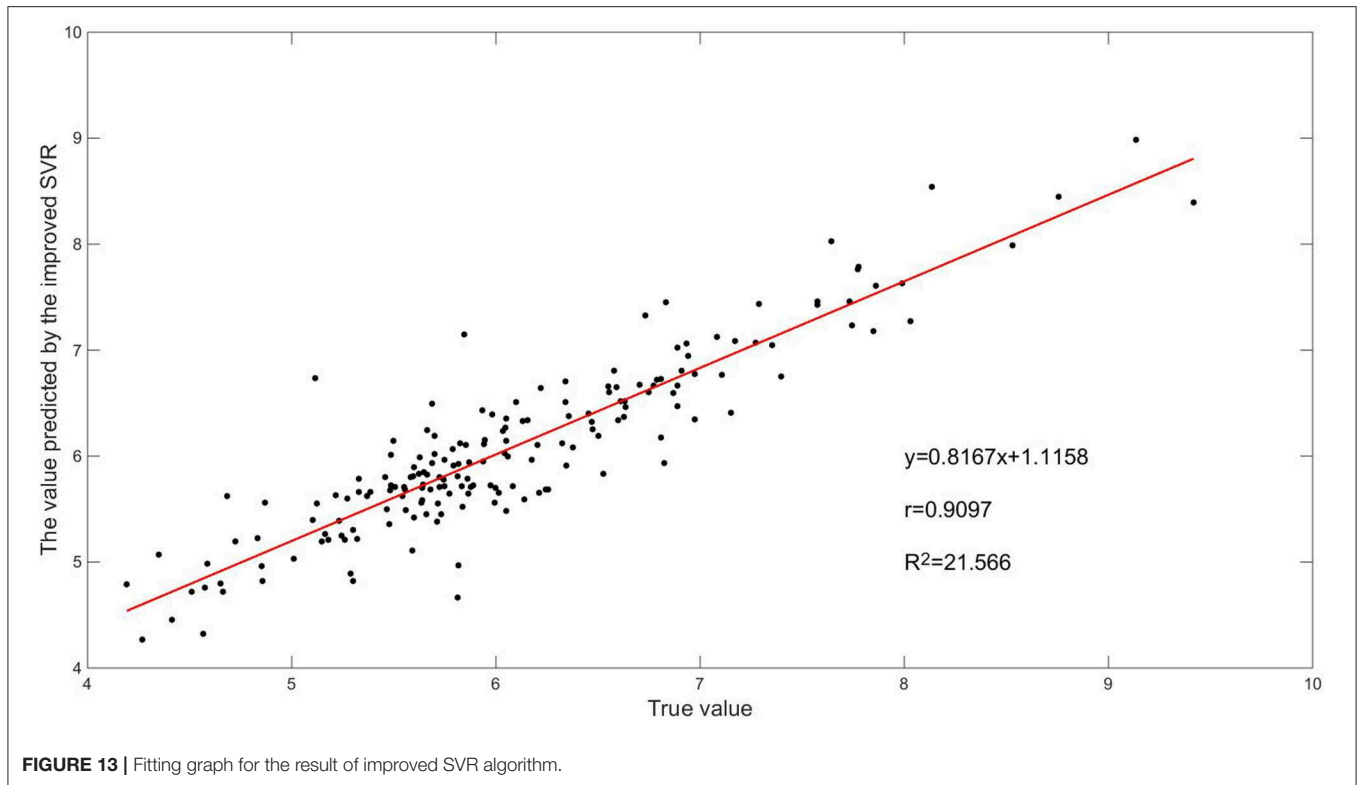
FIGURE 13 | Fitting graph for the result of improved SVR algorithm.

which has certain reference significance for the study of the evaporation ducts.

However, evaporation duct heights have a significant seasonal variation, which is not discussed in this paper. Therefore, future work will be applied to predicting the seasonal characteristics of evaporation ducts. In addition, when predicting, the regression function expression $f(x)$ obtained by the improved SVR algorithm is fixed and not updated with new observation data, that is, $f(x)$ is "static." In future work, a "dynamic" $f(x)$ will be introduced, to enhance the prediction model of atmospheric ducts using the real-time observation data, so as to further improve the accuracy of the predictions.

DATA AVAILABILITY STATEMENT

The high-resolution sounding data from the global positioning system are provided at https://www.sparc-climate.org. The SST data are available from www.ncc-cma.net.

AUTHOR CONTRIBUTIONS

ZS, YM, and CL design the improved SVR algorithm. LL provided the new diagnostic model of evaporation duct heights. All authors have contributed to the interpretation of the results and the preparation of the manuscript. All authors read and approved the final manuscript.

FUNDING

ACKNOWLEDGMENTS

REFERENCES

Babin, S. M., and Dockery, G. D. (2002). LKB-based evaporation duct model comparison with buoy data. *J. Appl. Meteorol.* 41, 434–446. doi: 10.1175/1520-0450(2002)041<0434:Lbedmc>2.0.Co;2

Babin, S. M., Young, G. S., and Carton, J. A. (1997). A new model of the oceanic evaporation duct. *J. Appl. Meteorol.* 36, 193–204. doi: 10.1175/1520-0450(1997)036<0193:ANMOTO>2.0.CO;2

Bankert, R. L., Hadjimichael, M., Kuciauskas, A. P., Richardson, K. L., Turk, J., Hawkins, J. D., et al. (2002). "Automating the estimation of various meteorological parameters using satellite data and machine learning techniques," in *Igarss 2002: IEEE International Geoscience and Remote Sensing Symposium and 24th Canadian Symposium on Remote Sensing, Vols. I–VI, Proceedings: Remote Sensing: Integrating Our View of the Planet* (Toronto. ON).

Basak, D., Srimanta, P., and Patranbis, D. C. (2007). Support vector regression. *Neural Inform. Process. Lett. Rev.* 11, 203−224. doi: 10.1007/978-1-4302-5990-9_4

Burk, S. D., Haack, T., Rogers, L. T., and Wagner, L. J. (2003). Island wake dynamics and wake influence on the evaporation

duct and radar propagation. *J. Appl. Meteorol.* 42, 349–367. doi: 10.1175/1520-0450(2003)042<0349:IWDAWI>2.0.CO;2

Chang, S., Sheng, Z., Du, H., Ge, W., and Zhang, W. (2020). A channel selection method for hyperspectral atmospheric infrared sounders based on layering. *Atmos. Meas. Tech.* 13, 629–644. doi: 10.5194/amt-13-629-2020

Czernecki, B., Nowosad, J., and Jablonska, K. (2018). Machine learning modeling of plant phenology based on coupling satellite and gridded meteorological dataset. *Int. J. Biometeorol.* 62, 1297–1309. doi: 10.1007/s00484-018-1534-2

Ebtehaj, I., and Bonakdari, H. (2016). A support vector regression-firefly algorithm-based model for limiting velocity prediction in sewer pipes. *Water Sci. Technol.* 73, 2244–2250. doi: 10.2166/wst.2016.064

Fairall, C. W., Bradley, E. F., Hare, J. E., Grachev, A. A., and Edson, J. B. (2003). Bulk parameterization of air-sea fluxes: Updates and verification for the COARE algorithm. *J. Clim.* 16, 571–591. doi: 10.1175/1520-0442(2003)016<0571:Bpoasf>2.0.Co;2

Ham, Y.-G., Kim, J.-H., and Luo, J.-J. (2019). Deep learning for multi-year ENSO forecasts. *Nature* 573, 568–572. doi: 10.1038/s41586-019-1559-7

He, X., Guo, J., Wu, J., Li, X., Tian, B., Zhong, Y., et al. (2018). Short-term forecast for evaporation duct height based on time series. *J. Electron. Meas. Instrum.* 32, 102–103. doi: 10.13382/j.jemi.2018.01.014

He, Y., Sheng, Z., and He, M. (2020). Spectral analysis of gravity waves from near space high-resolution balloon data in Northwest China. *Atmosphere* 11:133. doi: 10.3390/atmos11020133

Huang, J. (2004). "The analysis of time series," in *The Meteorological Statistical Analysis and Forecast Method, 3rd Edn*, ed R. Zhang (Beijing: Meteorology Press), 195–198.

Ivanov, V. K., Shalyapin, V. N., and Levadnyi, Y. V. (2007). Determination of the evaporation duct height from standard meteorological data. *Izvestiya Atmos. Ocean. Phys.* 43, 36–44. doi: 10.1134/s0001433807010045

Kang, S., Zhang, Y., and Wang, H. (2014). "The characteristics and detection of atmospheric duct," in *Atmospheric Ducts in the Troposphere, 3rd Edn*, ed Z. Wang (Beijing: Science Press), 44–53.

Lee, M.-K., Moon, S.-H., Kim, Y.-H., and Moon, B.-R. (2014). "Correcting abnormalities in meteorological data by machine learning," in: *2014 IEEE International Conference on Systems, Man and Cybernetics. IEEE International Conference on Systems Man and Cybernetics Conference Proceedings* (San Diego, CA: IEEE), 888–893.

Li, Y., Gao, Z., Li, D., Chen, F., Yang, Y., and Sun, L. (2015). An update of non-iterative solutions for surface fluxes under unstable conditions. *Bound. Layer Meteorol.* 156, 501–511. doi: 10.1007/s10546-015-0032-x

Li, Y., Gao, Z., Li, D., Wang, L., and Wang, H. (2014). An improved non-iterative surface flux scheme for atmospheric stable stratification conditions. *Geosci. Model Dev.* 7, 515–529. doi: 10.5194/gmd-7-515-2014

Liu, C., Huang, J., and Jiang, C. (2001). Modeling evaporation duct over sea with pseudo-refractivity and similarity theory. *Acta. Electronica. Sinica.* 29, 107–109. doi: 10.3321/j.issn:0372-2112.2001.07.030

Liu, L., Li, Y., Gao, Z., Bi, X., and Chen, Q. (2017). The prediction model of evaporation duct based on non iterative sea air flux algorithm. *J. Appl. Oceanogr.* 36, 23–25.

Liu, L., Li, Y., Gao, Z., Bi, X., and Zhu, G. (2019). Comparison and analysis of four kinds of evaporation duct model. *J. Meteorol. Sci.* 39, 82–96. doi: 10.3969/2017jms.0037

Mai, Y., Sheng, Z., Shi, H., Liao, Q., and Zhang, W. (2020). Spatiotemporal distribution of atmospheric ducts in Alaska and its relationship with the Arctic vortex. *Int. J. Antennas Propag.* 2020, 1–13. doi: 10.1155/2020/9673289

Neto, E. D., de Carvalho, F. A. T. and, Tenorio, C. P. (2004). "Univariate and multivariate linear regression methods to predict interval-valued features," in *Ai 2004: Advances in Artificial Intelligence,in Proceedings*, Vol. 3339, eds G. I. Webb and X. Yu (Cairns), 526–537. https://doi.org/10.1007/978-3-540-30549-1_46

Paulson, C. A. (1970). The mathematical representation of wind speed and temperature profiles in the unstable atmospheric surface layer. *Appl. Meteorol.* 9, 857–861. doi: 10.1175/1520-0450(1970)009<0857:TMROWS>2.0.CO;2

Paulus, R. A. (1985). Practical application of an evaporation duct model. *Radio Sci.* 20, 887–896. doi: 10.1029/RS020i004p00887

Rhee, J., and Im, J. (2017). Meteorological drought forecasting for ungauged areas based on machine learning: using long-range climate forecast and remote sensing data. *Agric. For. Meteorol.* 237, 105–122. doi: 10.1016/j.agrformet.2017.02.011

Serrurier, M., and Prade, H. (2008). Improving inductive logic programming by using simulated annealing. *Inform. Sci.* 178, 1423–1441. doi: 10.1016/j.ins.2007.10.015

Sheng, Z., and Huang, S.-X. (2009). Ocean duct inversion using radar clutter and its noise restraining ability. *Acta Phys. Sin.* 58, 4328–4334. doi: 10.1360/972008-2465

Sheng, Z., and Huang, S.-X. (2010). Ocean duct inversion from radar clutter using variation adjoint and regularization method (II): inversion experiment. *Acta Phys. Sin.* 59, 3912–3916. doi: 10.7498/aps.59.3912

Shi, Y., Zhang, Q., Wang, S., Yang, K., Yang, Y., Yan, X., et al. (2019). A comprehensive study on maximum wavelength of electromagnetic propagation in different evaporation ducts. *IEEE Access* 7, 82308–82319. doi: 10.1109/access.2019.2923039

Tag, P. M., and Peak, J. E. (1996). Machine learning of maritime fog forecast rules. *J. Appl. Meteorol.* 35, 714–724. doi: 10.1175/1520-0450(1996)0352.0.CO;2

Tian, B., Cha, H., and Zhang, Y. (2009a). Study on the applicability of evaporation duct model A in Chinese sea areas. *Chinese J. Radio Sci.* 24, 176–181.

Tian, B., Yu, S., Li, J., and Jiang, H. (2009b). Study on the applicability of PJ evaporation duct model in semitropical sea areas. *Ship Sci. Technol.* 31, 99–102.

Twiddle, J. A., Spurgeon, S. K., Kitsos, C., and Jones, N. B., Ieee (2006). "A discrete-time Sliding Mode Observer for estimation of auto-regressive model coefficients with an application in condition monitoring," in *2006 International Workshop on Variable Structure Systems* (Alghero).

Wang, W., Guan, M., Tian, W., Schmidt, T., and Ding, A. (2019). Large uncertainties in estimation of tropical tropopause temperature variabilities due to model vertical resolution. *Geophys. Res. Lett.* 46, 10043–10052. doi: 10.1029/2019GL084112

Wang, Y., Wu, D. L., Guo, C. X., Wu, Q. H., Qian, W. Z., and Yang, J. (2010). "Short-term wind speed prediction using support vector regression," in *IEEE Power and Energy Society General Meeting 2010. IEEE Power and Energy Society General Meeting PESGM* (Providence, RI).

Xie, F., Li, J., Zhang, J., Tian, W., Hu, Y., Zhao, S., et al. (2017). Variations in north Pacific sea surface temperature caused by Arctic stratospheric ozone anomalies. *Environ. Res. Lett.* 12:114023. doi: 10.1088/1748-9326/aa9005

Xue, S., Yang, M., Li, C., et al. (2009). "Meteorological prediction using support vector regression with genetic algorithms[C]," in *International Conference on Information Science and Engineering* (Nanjing: IEEE). doi: 10.1109/ICISE.2009.735

Yang, S., Li, X., and Wu, J. (2016). Adaptability research of evaporation duct predication model based on NPS model. *J. Electron. Meas. Instrum.* 30, 1899–1906. doi: 10.13382/j.jemi.2016.12.013

Yu, G., Liu, A., and Yang, Y. (2015). Babin model of evaporation waveguide diagnosis and its sensitivity analysis. *J. Astron. Metrol. Meas.* 35, 53–56. doi: 10.3969/j.issn.1000-7202.2015.02.015

Yuan, F., Kumar, U., and Galar, D. (2010). Reliability prediction using support vector regression. *Int. J. Syst. Assur. Eng. Manage.* 1, 263–268. doi: 10.1007/s13198-011-0040-2

Zhang, J., Tian, W., Chipperfield, M., Xie, F., and Huang, J. (2016). Persistent shift of the Arctic polar vortex towards the Eurasian continent in recent decades. *Nat. Clim. Change* 6, 1094–1099. doi: 10.1038/nclimate3136

Zhao, X., Sheng, Z., Li, J., and Wei, K. (2019). Determination of the "wave turbopause" using a numerical differentiation method. *J.Geophys. Res. Atmos.* 124, 10592–10607. doi: 10.1029/2019JD030754